JGR Space Physics

RESEARCH ARTICLE
10.1029/2021JA029892

Energetic Ions Downtail of the Reconnection Site

Joachim Birn[1,2], Michael Hesse[3], Andrei Runov[4], Drew L. Turner[5], Ian Cohen[5], and James A. Slavin[6]

[1]Center for Space Plasma Physics, Space Science Institute, Boulder, CO, USA, [2]Space Science and Applications, Intelligence and Research Division, Los Alamos National Laboratory, Los Alamos, NM, USA, [3]Science Directorate, NASA Ames Research Center, Moffett Field, CA, USA, [4]Department of Earth, Planetary, and Space Sciences, University of California, Los Angeles, CA, USA, [5]Space Exploration Sector, the Johns Hopkins Applied Physics Laboratory, Laurel, MD, USA, [6]Department of Climate and Space Sciences and Engineering, University of Michigan-Ann Arbor, Ann Arbor, MI, USA

Abstract Using combined MHD/test particle simulations, we explore characteristics of ion (proton) acceleration tailward of a near-Earth reconnection site. We present spatial distributions and explore acceleration mechanisms and sources of accelerated ions. Acceleration is due primarily due simple crossings of the enhanced electric field near the x-line or in the departing plasmoid. The energetic particle distributions show the expected energy dispersed tailward streaming at the plasma sheet boundary, while equatorial distributions are more complicated, resulting from different acceleration sites within the moving plasmoid. Sources are mostly inside the central plasma sheet dawnward of the plasmoid.

Key Points:

- Energetic ion fluxes form tailward beams surrounding the plasmoid but multiple separate branches near the equatorial plane
- Boundary beams are primarily accelerated near *x*-line, equatorial acceleration occurs anywhere across tailward propagating plasmoid
- Origins of accelerated ions are primarily in the downward central plasma sheet

Correspondence to:
J. Birn,
jbirn@spacescience.org

Citation:
Birn, J., Hesse, M., Runov, A., Turner, D. L., Cohen, I., & Slavin, J. A. (2022). Energetic ions downtail of the reconnection site. *Journal of Geophysical Research: Space Physics*, *127*, e2021JA029892. https://doi.org/10.1029/2021JA029892

Received 17 AUG 2021
Accepted 25 DEC 2021

1. Introduction

The Earth's magnetotail plays a prominent role in the dynamics of the magnetosphere, as a site of temporary energy storage and sudden release, involving magnetic reconnection and causing ground disturbances and auroral displays. Its different regions are here denoted as follows:

"Near tail" denotes the region earthward of about 25–30 Earth radii (R_E) down to geosynchronous orbits, which includes the region where, according to standard substorm models, a new reconnection site forms, governing substorm and other activity. This region has been explored most recently by the satellite missions Cluster (Escoubet et al., 2001), "Time History of Events and Macroscale Interactions during Substorms" (THEMIS) (Angelopoulos, 2008), and "Magnetospheric Multiscale" (MMS) (Burch et al., 2016). Earlier observations by "Orbiting Geophysical Observatory" (OGO) and Vela satellites in this region, together with ground magnetic observations, have laid the basis for the now widely accepted "Near-Earth Neutral Line" model of substorms (Baker et al., 1996; Hones, 1977; McPherron et al., 1973), which states that substorm features are closely related to the formation of reconnection in this region, associated with earthward and tailward plasma flows, a collapse ("dipolarization") of the inner tail, and the severance of a portion of the plasma sheet and its ejection as a plasmoid. Essential elements of this model had already been suggested by Atkinson (1966) and Atkinson (1967).

"Far tail," "deep tail," or "distant tail" denotes the region beyond the distance of the Moon, which has been explored until recently only by two satellite missions, "International Sun-Earth Explorer"-3 (ISEE-3) (Bame et al., 1983; Baker, et al., 1984; Hones, 1977; Slavin et al., 1983; Tsurutani et al., 1984; Tsurutani & von Rosenvinge, 1984; Zwickl et al., 1984) and Geotail (Kokubun et al., 1994; Machida et al., 1994; Mukai et al., 1994; Nishida, 1994). This region typically includes a "distant neutral line" (Hones, 1977; Baker et al., 1984), which is considered to terminate the region of closed field lines, which are connected to Earth at both ends during quiet times, and may also be the site of reconnection.

The region in between is termed here "mid tail." It covers the region of the departing plasmoids (e.g., Galeev, 1979; Hones, 1977), potential earthward flows from the distant neutral line (e.g., Kiehas et al., 2018), but may also be the site of, presumably reconnection related, local activity (Sergeev et al., 1996). This region is the main region of interest in the present investigation, although our results may be pertinent also for the more distant magnetotail. It was first explored by Explorer satellites (also labeled "International Monitoring Platform," IMP) with Explorers 33 and 35 being the first satellites to establish the tail magnetic geometry out to and beyond the distance of the Moon (Behannon, 1968; Mihalov & Sonett, 1968; Ness et al., 1967a, 1967b). Mihalov et al. (1968) established the persistence of a magnetic field component normal to the neutral sheet, taking the occasional southward turning as evidence of reconnection earthward from the satellites. Armstrong and Krimigis (1968) and Fennell (1970)

reported Explorer 33 and 35 observations of proton bursts with energies above 0.31 MeV in the tail region out to and beyond the Moon's distance. These flows were preferentially, but not always, anti-earthward, mostly aligned with the magnetic field, and closely related to auroral bay activity.

Based on IMP-7 observations at $\sim 35 R_E$ distance, Sarris, Krimigis, & Armstrong (1976) identified proton bursts with energies above 0.29 MeV (and electron bursts with $E_e \geq 0.22$ MeV) in the plasma sheet (as well as in the boundary layer and the magnetosheath). The bursts showed anisotropies both toward and away from Earth together with a significant dawn-to-dusk component and also an association with magnetic activity. Sarris, Krimigis, Iijima, et al. (1976) reported IMP-6 and IMP-7 observations of proton bursts near $x_{SM} \approx -32 R_E$ in association with a substorm, indicating a nearby source with a location first tailward, then earthward of the satellites.

On the basis of ISEE-3 data, Scholer et al. (1983) found that suprathermal protons with energies above ~35 keV are a persistent feature of the distant tail and Daly et al. (1984), without distinguishing between quiet and disturbed times, found an almost equal occurrence of tailward and earthward streaming energetic ions above 35 keV at distances below $\sim 100\ R_E$ but a strong preponderance of tailward streaming beyond. Cowley et al. (1984) also reported energetic ions streaming mainly tailward, particularly in boundary layers of the distant plasma sheet. ISEE-3 observations in the far tail (Baker, et al., 1984; Hones, 1977; Richardson & Cowley, 1985; Richardson et al., 1987; Scholer, Gloeckler, Hovestadt, et al., 1984; Scholer, Gloeckler, Klecker, et al., 1984) provided a detailed description of energetic particle properties associated with plasmoids, showing energy dispersed energetic ions streaming tailward along the magnetic field at the boundary of tailward moving plasmoids, while the interior was characterized by more broadly distributed, apparently tailward convecting populations. (The ion plasma instrument on ISEE-3 was not functioning during the far tail mission).

The conclusions from ISEE-3 observations were confirmed and expanded by ion plasma observations of Geotail (e.g., Håland et al., 1999; Ieda et al., 1998; Machida et al., 2000; Nagai et al., 1994) and the, lunar orbiting, Acceleration, Reconnection, Turbulence, and Electrodynamics of Moon's Interaction with the Sun (ARTEMIS) spacecraft (Angelopoulos, 2011). Runov et al. (2018) conducted a statistical analysis of tailward reconnection outflows captured by the ARTEMIS probes. They showed that typical ion energy spectra obtained in the outflows are characterized by increased fluxes at energies above 10 keV compared to the ion spectra in the background plasma sheet, while the spectral shape was non-Maxwellian with a pronounced high energy tail. Grigorenko et al. (2019) studied ion and electron beams observed by the ARTEMIS probes near the plasma sheet boundary layer (PSBL). They found no significant differences in characteristics between earthward and tailward ion beams, nor between beams observed on open or closed field lines. However, tailward ion beams tended to be shorter and more closely related to high absolute values of the AL index, that is, geomagnetic activity.

A few attempts have been made to model the acceleration and fluxes of energetic ions in the mid and distant tail. The large extent of the region of interest from the near-Earth reconnection site to the distance of the Moon and beyond obviously does not permit a fully self-consistent particle simulation. Zeleny et al. (1984) and Zelenyi et al. (1990) used a largely analytic approach to address the ion and electron acceleration in the vicinity of an x-line, based on the explosive growth of a tearing mode (Galeev, 1979) in a two-dimensional configuration, neglecting variations in the cross-tail (y) direction. They demonstrated efficient acceleration from the inductive electric field and the formation of power-law high-energy distributions.

Investigations that have taken the large-scale tail structure into account have used a combination of MHD simulation with test particle tracing in the fields of this simulation. In particular, Scholer and Jamitzky (1987) and Scholer and Jamitzky (1989) used a two-dimensional MHD simulation of near tail reconnection and plasmoid ejection to study the acceleration of protons in the electric and magnetic fields of the simulation. In their simulations, energized protons originated from the lobes at various distances in x and were accelerated in the vicinity of the near-Earth x-line. The subsequent motion toward the distant tail lead to strongly field-aligned fluxes close to the plasma sheet boundary with the expected spatial dispersion of the largest energies closest to the boundary.

Birn et al. (2004) followed a similar approach, however, based on a three-dimensional MHD simulation (Birn & Hesse, 1996). They focused particularly on the acceleration of O^+ ions, but included also results on H^+ ions, at a single final energy of 180 keV. They also found the resulting energetic ion fluxes concentrated close to the plasma sheet boundary. However, the particles originated not only from the lobes but, to a significant amount, from inside the plasma sheet dawnward of the observation site.

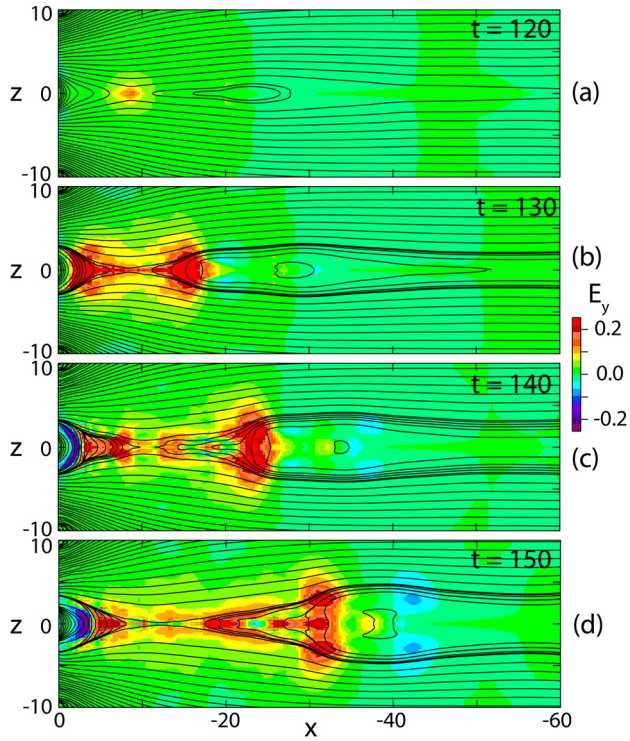

Figure 1. Evolution of the (normalized) electric field component E_y (color) in the x, z plane. Black lines again are magnetic flux contours.

Here we use a similar procedure, based on the three-dimensional, time-dependent fields of an MHD simulation of near-tail reconnection, flow bursts, and plasmoid ejection (Birn et al., 2011). In contrast to the earlier MHD simulation (Birn & Hesse, 1996), this simulation also includes a transition toward a dipole field, a significantly lower plasma pressure in the lobes of ~ 0.5% of the typical lobe magnetic pressure, and a small net cross-tail magnetic field component of ~ 1% of the lobe magnetic field strength. We will focus particularly on two specific energies and on the tail region inside but close to the Moon's distance, as explored by the ARTEMIS satellites.

It should be noted that our investigation, due to the properties of the underlying MHD simulation, pertains to large-scale plasmoids of several tens of R_E lengths in the Sun-Earth (x) direction, as inferred, for instance, by Hones, Birn, et al. (1984) (75–150 R_E) or Scholer, Gloeckler, Hovestadt, et al. (1984) (50–100 R_E) on the basis of ISEE-3 observations out to ~220 R_E. This length represents the typical length of closed loops or helical field lines resulting from single x-line reconnection in the near tail combined with a distant x-line beyond the Moon's distance; it provides an upper limit of observed scales. Statistical analyses (Moldwin & Hughes, 1992), based on ISEE-3 measurements in the near and distant tail, revealed average lengths of 16.7 ± 13.0 R_E while Geotail data in the nearer tail inside of ~30 R_E yielded plasmoid sizes of 3–9 R_E (Håland et al., 1999) and ~4.4 R_E (Slavin et al., 2003). Recent MMS observations indicated plasmoids or flux ropes of even shorter scales of a few ion inertial lengths (Eastwood et al., 2007; Sun et al., 2019), corresponding to x dimensions of ~1,500 km or less.

There is evidence that large-scale plasmoids move from the near and mid tail to the distant tail (e.g., Angelopoulos et al., 1995; Richardson et al., 1987; Slavin et al., 1998, 1999). However, it is not clear how small-scale islands or flux ropes evolve, whether they form prior to merging into big islands or from break-up of larger ones, and whether they maintain their identity between the near and the far tail. Both, particle-in-cell (PIC) and resistive MHD simulations have shown that long, stretched thin current sheets may develop small-scale magnetic islands, which subsequently merge into larger ones (e.g., Bhattacharjee et al., 2009; Daughton et al., 2009). However, these simulations typically start from assuming very thin extended current sheets, which may represent an early state prior to the major plasmoid ejection or the "postplasmoid plasma sheet" tailward of a large departing plasmoid (Richardson et al., 1987). Furthermore, little is known about the association of small-scale plasmoids with energetic particles. While there is some evidence that small-scale islands may be effective in accelerating electrons (Chen et al., 2008; Zhong et al., 2020), as suggested by Drake et al. (2006), a similar effect on ions has not been documented; most likely because their size is too small to trap and quasi-adiabatically affect ions.

2. MHD Results

The underlying MHD simulation is described in more detail by Birn et al. (2011). It spans a region $0 \geq x \geq -60$, $|y| \leq 40$, $|z| \leq 10$ with the Earth dipole located at $x = 5$, outside the box. As in earlier papers, we use a dimensional length unit $L_n = 1.5R_E$, choosing other dimensional units as $B_n = 12.6$ nT and $v_n = 1{,}000$ km/s. Here B_n denotes the lobe field strength and v_n an Alfvén velocity, based on B_n and the plasma sheet density, at $x \approx -10$, close to the location where the x-line forms in the simulation. The chosen units lead to a time unit $t_n = L_n/v_n \approx 10$ s and electric field $E_n = v_n B_n = 12.6$ mV/m.

After a period of external driving, causing the formation of a thin embedded current sheet, a dynamic evolution is initiated at $t = 61$ by imposing finite resistivity concentrated in the region of enhanced current density, while the driving is stopped. This leads to the start of weak reconnection at $t \approx 90$, followed by more rapid reconnection after $t \approx 120$.

Figures 1 and 2 provide an overview of the evolution of the cross-tail electric field in the $y = 0$ and $z = 0$ plane, respectively. (The Moon's distance would be close to the center of the box near $x = -35$.) This electric field

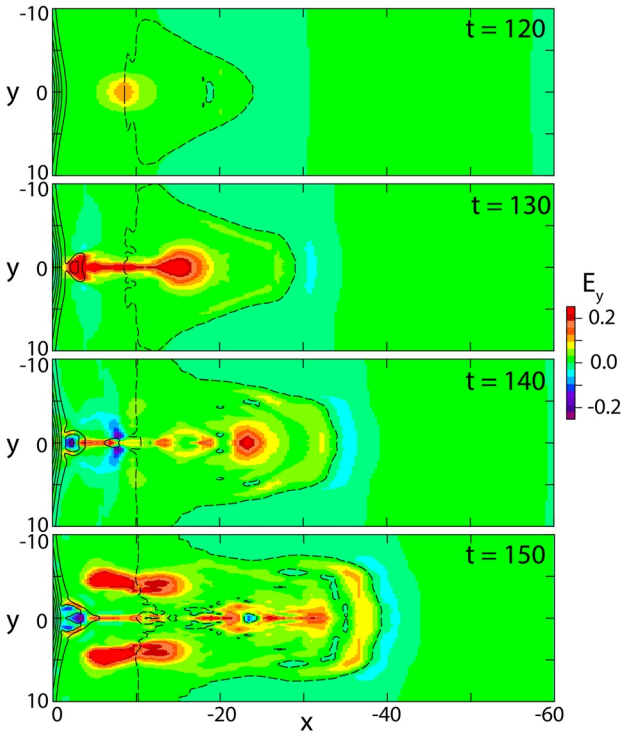

Figure 2. Evolution of the (normalized) electric field component E_y (color) in the x, y plane. Black lines are contours of constant B_z; $B_z = 0$ lines are dashed. The two blue lines in panel (b) are projections of field lines.

component, closely related to the fast earthward and tailward flows, is the dominant factor in the particle acceleration. The contribution to the total field from the resistive term is confined to the vicinity of the x-line. It is initially considerably smaller than the fields shown and would not show in the color scheme of Figures 1 and 2 but is increased at later times over the initial values by an intensification of current density associated with the dynamic evolution, which might be considered as nonlinear (resistive) tearing in a 3D geometry (Galeev, 1979; Schindler, 1974). As the application of an external field is discontinued after the initial driven phase, the electric field in the MHD simulation illustrated in Figures 1 and 2 can entirely be considered as inductive, resulting from $\partial \mathbf{B}/\partial t$.

Figure 2 shows the effects of rapid reconnection and fast flows first near midnight (t = 130, 140) and then (t = 150) near $|y| \approx 4$. It is noteworthy that the maximum cross-tail voltage difference $\int E_y dy$ tailward of the near-Earth reconnection site ($x \approx -10$) amounts to ~80 kV, based on our chosen units. This corresponds to a maximum energy of ~80 keV for a singly charged ion gained from a single crossing of the high E_y field.

Note also that, even before additional flow bursts arise outside of the first one near midnight, there is not a uniquely defined plasmoid width in y, as illustrated by the two field line projections in Figure 2b. The field line closer to the core of the plasmoid (dark blue line) extends over a wider distance in y than the field line closer to the plasmoid boundary (light blue line).

3. Orbit Integration

Proton orbits were integrated backward in time from selected final locations and final velocities on the basis of the time dependent magnetic and electric fields of the MHD simulation. The orbits were stopped when they reached the initial state (t = 61) or one of the outer boundaries. At the inner boundary, $x = 0$, particles were reflected back, however, taking into account a delay time consistent with mirroring closer to Earth, outside the simulation box. This time was estimated from motion in a Tsyganenko model field (Tsyganenko, 1987) that was matched to the inner boundary. Particle fluxes were evaluated by mapping the phase space density f from the initial to the final location, using Liouville's theorem of the conservation of f along a phase space trajectory (Curran & Goertz, 1989). Enhanced fluxes therefore are primarily due to large energy gains (low initial energies implying higher f values) and, to a minor extent the higher density in the source region, that is, central plasma sheet (CPS) versus PSBL or lobes.

Source distributions were chosen as kappa distributions (Christon et al., 1988, 1989; Vasyliunas, 1968),

$$f(W) \propto n_i \left(1 + \frac{W}{(\kappa - 3/2)kT_i}\right)^{-\kappa-1} \tag{1}$$

with W representing particle energy. The parameters n_i and T_i were chosen to be consistent with the pressure in the MHD simulation and $\kappa = 5.5$ was chosen on the basis of tail observations (Christon et al., 1988, 1989). We note, however, that the results reported below mostly reflect the energy gain along the orbits and would not be changed qualitatively if different source distributions (say, Maxwellians) or kappa values were chosen.

We used full orbit integration

$$\frac{d\mathbf{x}}{dt} = \mathbf{u} \qquad \frac{d\mathbf{u}}{dt} = \frac{eB_n t_n}{m}(\mathbf{E} + \mathbf{u} \times \mathbf{B}) \tag{2}$$

here $\mathbf{x}$ and $\mathbf{u}$ represent the particle location and velocity, normalized by L_n and v_n, respectively, m is the ion (here, proton) mass and e is the proton charge, while $\mathbf{E}$ and $\mathbf{B}$ are the normalized MHD fields, which were interpolated linearly in space and time from the finite grid of the MHD simulation. Since this could, in principle, lead to

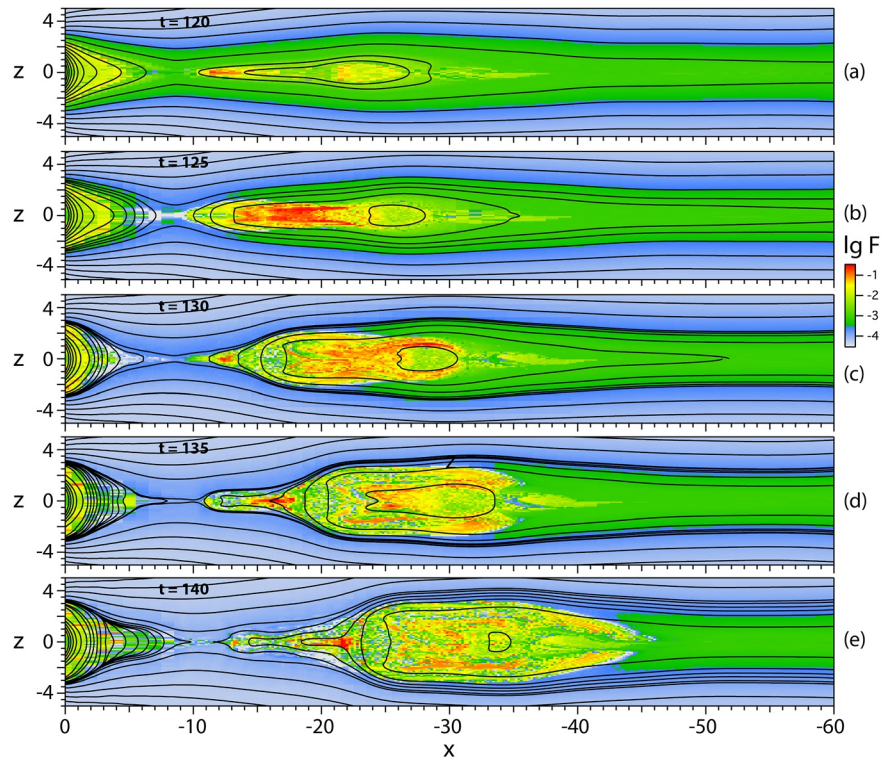

Figure 3. Tailward fluxes of 20.9 keV protons in the $y = 0$ plane.

spurious parallel electric fields, we did comparisons with an interpolation procedure that separated parallel and perpendicular electric field components and found that this effect was negligible for ion orbits.

Based on the velocity unit defined in Section 2, the proton energy is given by $W = W_n u^2$ where

$$W_n = \frac{1}{2} m v_n^2 = 5.22\,\text{keV} \tag{3}$$

we note that the orbit integration (2) depends only on q/m (with $q = e$ for protons), through the dimensionless parameter σ defined by

$$\sigma = \omega_{ci} t_n = \frac{q B_n}{m} t_n = \frac{L_n}{d_i} \tag{4}$$

where d_i is the ion (proton) inertial length, with $\sigma = 11.5$ for the chosen units. Multiplying the magnetic field unit by a factor λ and the time unit by $1/\lambda$, leaves σ unchanged. Leaving the length unit also unchanged, the orbit results can be applied also to a different parameter set with v_n multiplied by λ, and E_n and W_n by λ^2.

4. Evolution of Ion Fluxes

4.1. Midnight Meridional Plane

Figures 3 and 4 show the evolution of tailward fluxes of 20.9 and 83.5 keV (final energy), respectively, in the midnight meridional plane, $y = 0$. Each pixel corresponds to a single phase space trajectory backward from the given location to the source location (which in almost all cases was at the initial state $t = 61$) and the distribution function value f thus represents the value at the source location mapped to the final location, according to the procedure described in Section 3. The fluxes occupy the CPS closer to Earth but split into two layers surrounding the plasmoid core at later times and larger distances. As expected and observed, the higher-energy fluxes are at higher latitude, somewhat closer to the plasmoid boundary. Remarkably, at later times and larger distance, the boundary fluxes at higher energy converge around the front of the plasmoid toward the equatorial plane. In the

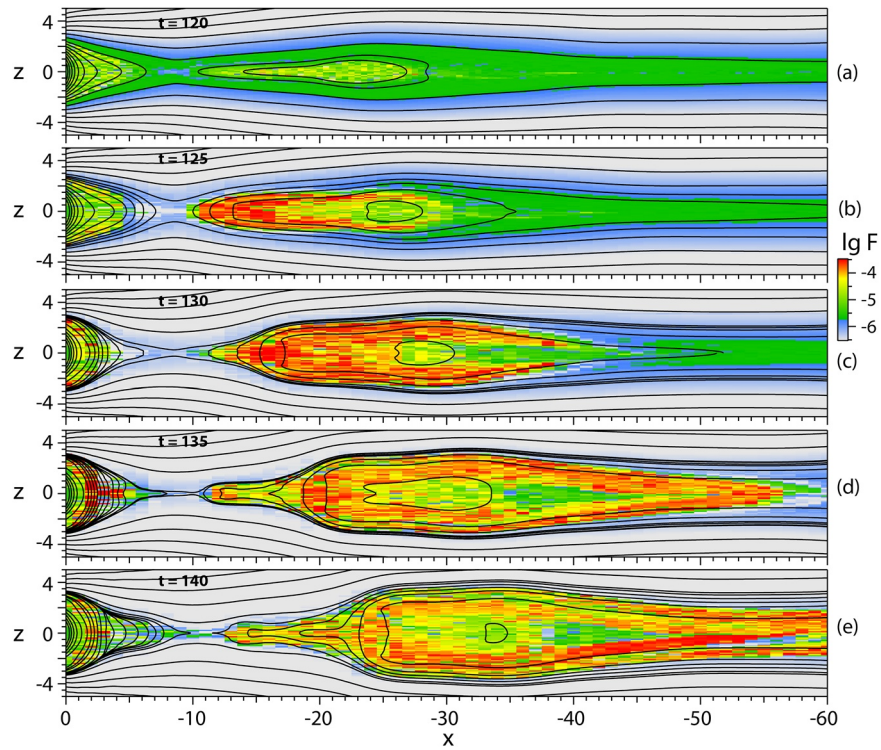

Figure 4. Same as Figure 3 but for 83.5 keV energy.

present simulation and based on the chosen dimensional units, this happens at a distance beyond the Moon's. However, this result might vary depending on characteristic length and velocity scales.

4.2. Equatorial Plane

Figures 5 and 6 show the evolution of the tailward fluxes in the equatorial plane, $z = 0$, together with the projections of several orbits contributing to the enhanced fluxes, shown as multi-colored lines. The color of these lines indicate the instantaneous energy W corresponding to the color bars on the lower right in Figure 5 and the top right in Figure 6. The green portions, in particular, indicate where the dominant energy increase occurs

The regions of enhanced fluxes show a complicated structure, which involves multiple regions, and changes in time. The enhanced fluxes tend to be shifted toward dusk as expected from the duskward acceleration. However, at times enhanced fluxes may also extend dawnward, for instance at $t = 130$ for 20.9 keV (Figure 5c) near $x \approx -15$. In this case, the effect appears to be related to an expansion of the region of enhanced electric field E_y (and the associated flow) from a narrow channel closer to the x-line as indicated by the black contours. The sample orbits in Figure 5c that end on the dawn side indicate that the flux enhancements also result from single crossings of the enhanced electric field in the y direction. As one might expect, this effect is less pronounced at higher energies (Figure 6). Figures 6d and 6e also show the sudden appearance of fluxes at large distance, $x \approx -50$ and beyond, which is related to the convergence of the fluxes toward the equatorial plane shown in Figures 4d and 4e.

4.3. Cross-Sectional $x = -30$ Plane

Figure 7 shows the evolution of tailward fluxes of 20.9 and 83.5 keV in the center of the box, $x = -30$, as function of y and z. Black and red contours indicate topological boundaries. The red lines show the outer boundary of closed plasmoid field lines and the black lines the inner lobe boundary. The region between the red and the black lines in the center corresponds to open, disconnected field lines, resulting from lobe field reconnection, whereas the region farther away in $|y|$ correspond to closed field lines, extending into the more distant tail, which have not (yet) undergone reconnection. Overall the region of energetic particle fluxes show a shape of a lying U, extending

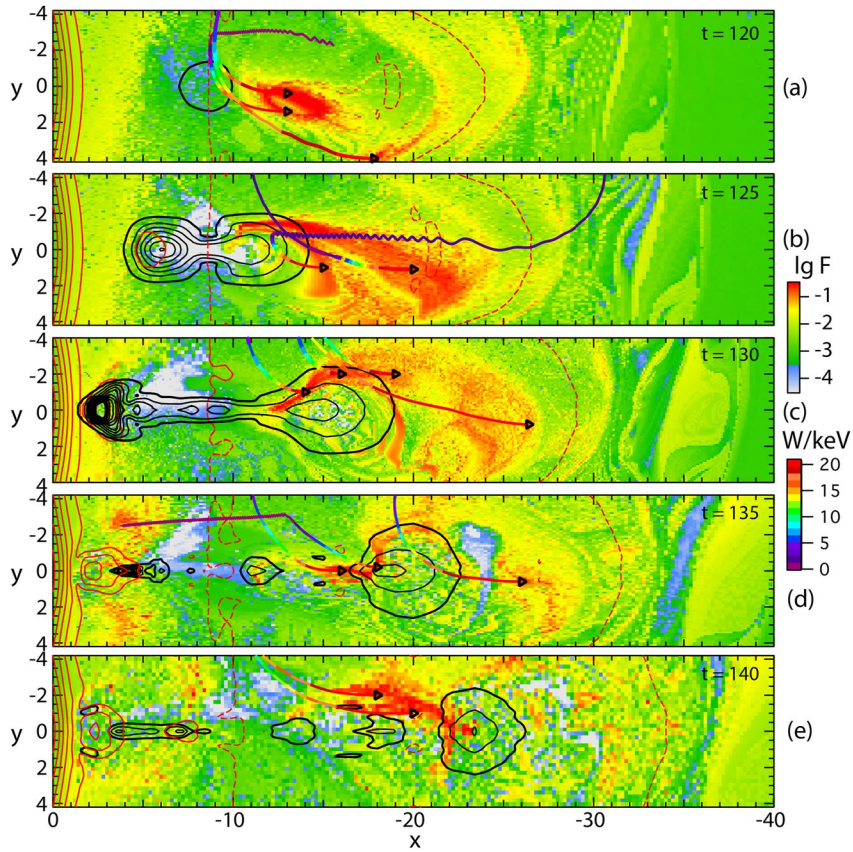

Figure 5. Tailward fluxes of 20.9 keV protons in the $z = 0$ plane at various times indicated in the top right of each panel. Black contours indicate enhanced cross-tail electric field, and red contours are contours of constant B_z, as shown in Figure 2, with the $B_z = 0$ lines shown as dashed lines. The multi-colored lines show projections of typical orbits of protons contributing to the enhanced fluxes with the color indicating the instantaneous energy corresponding to the lower scale on the right. The black triangles show the final particle locations.

duskward and toward the boundary regions near midnight. The outer separatrix (black lines) encloses the region of accelerated particles with the region of more energetic particles closer to the boundaries but the boundary between closed plasmoid fields and open disconnected field lines (red lines) apparently does not affect the energetic particle fluxes. However, this may be the result of our MHD configuration, which has no distinct drop in pressure or density at the open/closed boundary.

The origins of the accelerated particles shown in Figures 7c and 7g at $t = 130$ are indicated in Figures 8a and 8b, selecting the pixels with the largest fluxes. The origins are colored according to the initial pressure at $t = 61$, as indicated by panel *c*. The 20.9 keV particles (Figure 8a) all originate from the inner (red) and outer (orange pixels) CPS, while for 83.5 keV (Figure 8b) the PSBL contributes as well (green pixels). These contributions are well ordered, proceeding duskward and outward with the sources proceeding from inner CPS toward outer CPS and PSBL. It is noteworthy that the boundaries between these source regions are not related to the boundary between closed plasmoid and disconnected field lines (red lines) at this time.

Figures 8d and 8e show the source locations in x and z of the particles contributing to the peak fluxes. The color now indicates the relative energy gain of the particles. This shows that particles with the higher energy gain tend to come from the more distant tail for 83.5 keV (orange and red pixels in Figure 8e) while the source locations are more mixed for 20.9 keV (Figure 8d).

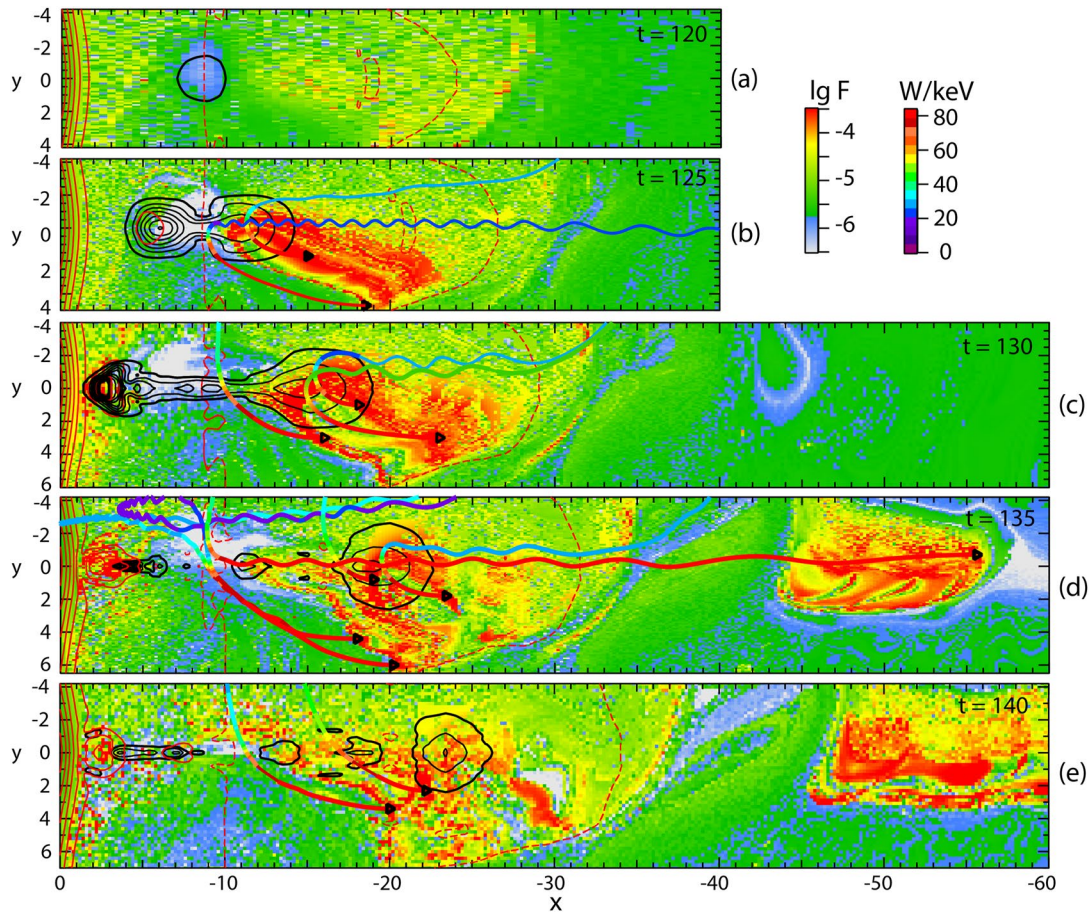

Figure 6. Same as Figure 5 but for 83.5 keV energy.

5. Typical Orbits and Acceleration Mechanisms

The orbits shown in Figures 5 and 6 already illustrate that the energy gain typically results from a single crossing of the enhanced electric field region; the acceleration region primarily correspond to the part of the orbits colored in green. The acceleration may be close to the x-line, near $x = -10$, or farther tailward within the departing plasmoid. Here we illustrate two orbits in more detail.

Figure 9 shows two characteristic orbits (dark and light blue lines with final locations indicated by small triangles) contributing to the enhanced 20.9 keV fluxes at $t = 135$, as shown in Figures 3d and 5d, superposed on the color-coded electric field E_y at the final time. Figure 9a shows projections of the orbits into the x, y plane, Figure 9b in the x, z plane. The bottom panel, Figure 9c shows the energy as function of location x. It clearly demonstrates that the acceleration occurs by single crossings of the acceleration region of enhanced cross-tail electric field, close to the x-line for orbit B (light blue) but farther tailward in the moving plasmoid for orbit A (dark blue line). In either case the initial energy is near or below the thermal energy $W_n = 5.2$ keV. As shown by panel b, orbit B represents a particle contributing to the beams on the outside of the plasmoid near the boundary, while the particle of orbit A contributes to the equatorial fluxes.

Figure 10 illustrates two representative orbits of accelerated ions of 83.5 keV final energy. Both ions originate from the CPS on meandering orbits but from different distances. Particle D (light blue line) is characteristic for those contributing to the enhanced flux around $x \approx -50$, resulting from the convergence of boundary layer fluxes toward the equatorial plane. As illustrated by panel b, this particle in fact contributes to the boundary fluxes at earlier times. Panel c demonstrates that the particle energy is almost entirely field-aligned after cross-tail acceleration near the x-line at $x \approx -10$ before it converges toward $z = 0$ and becomes perpendicular when it reaches the equatorial plane (dark blue dashed line).

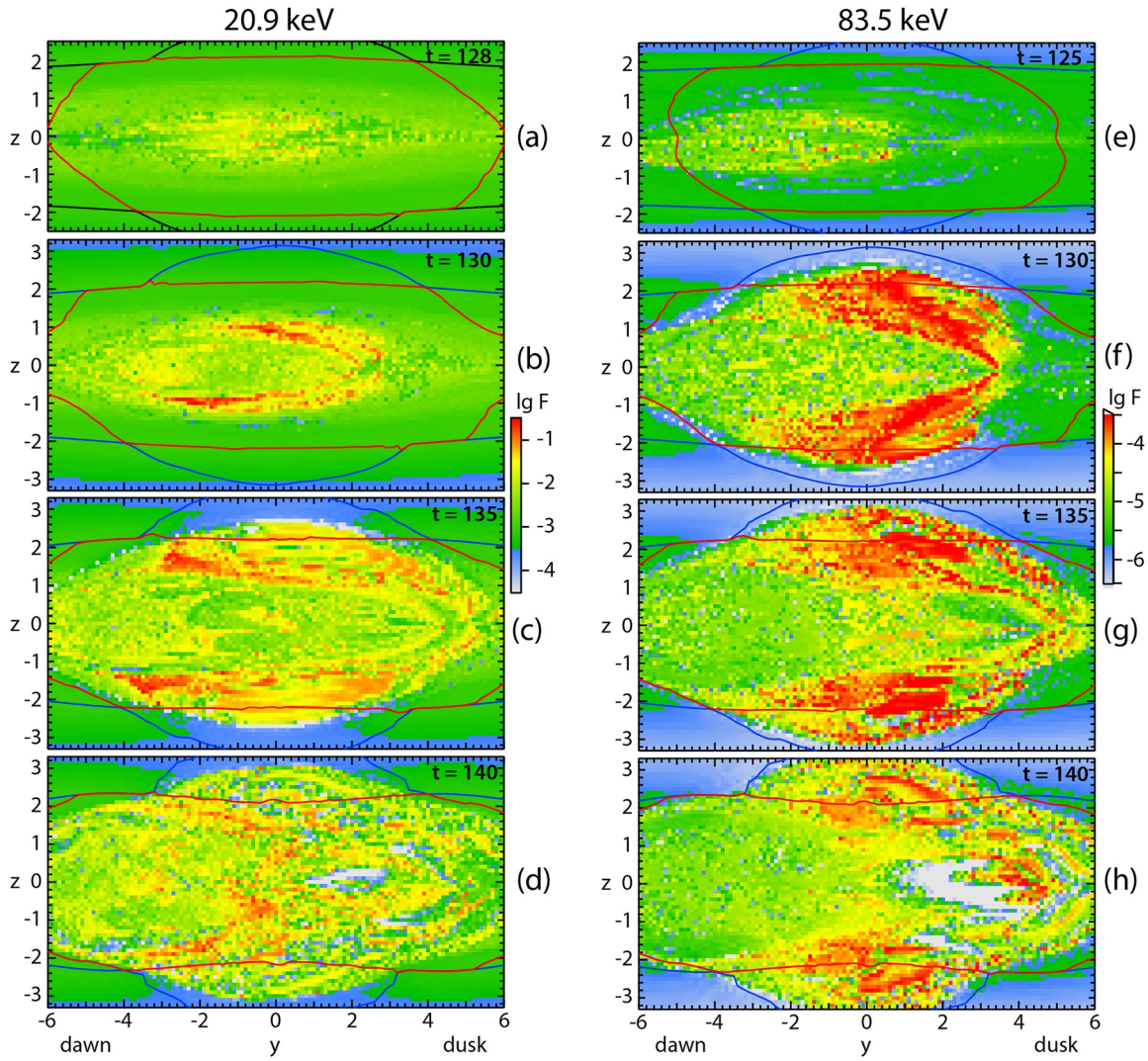

Figure 7. Tailward fluxes of 20.9 and 83.5 keV protons in the $x = -30$ plane. Black and red contours indicate topological boundaries with the red line showing the outer boundary of closed plasmoid field lines and the black line the inner lobe boundary.

In contrast, particle C (dark blue line) originates from a more distant location in x and becomes accelerated when it encounters the enhanced electric field of the departed plasmoid near ≈ -20. In both cases the initial energy is ~30 keV, consistent with the fact that the maximum gain by a simple crossing of the acceleration region should be less than about 80 keV.

All sample orbits shown so far demonstrate the same acceleration mechanism, a simple, non-adiabatic, crossing of a region of enhanced cross-tail electric field, either near the x-line in the near tail or within the departing plasmoid. This provides a maximum for the possible acceleration of ~80 keV, based on the chosen parameters, but more typically 50 keV or less.

6. Summary and Discussion

We have used our combined MHD/test particle approach to explore the acceleration and flux increases of hydrogen ions in the mid tail region tailward of a near-Earth reconnection site. External driving is used in the MHD simulation only to prepare the tail for reconnection by the formation of a thin embedded current sheet in the near tail. This driving is discontinued after finite resistivity is imposed in the region of the thin current sheet to enable reconnection; hence the simulation does not include a general externally driven convection. Our simulation

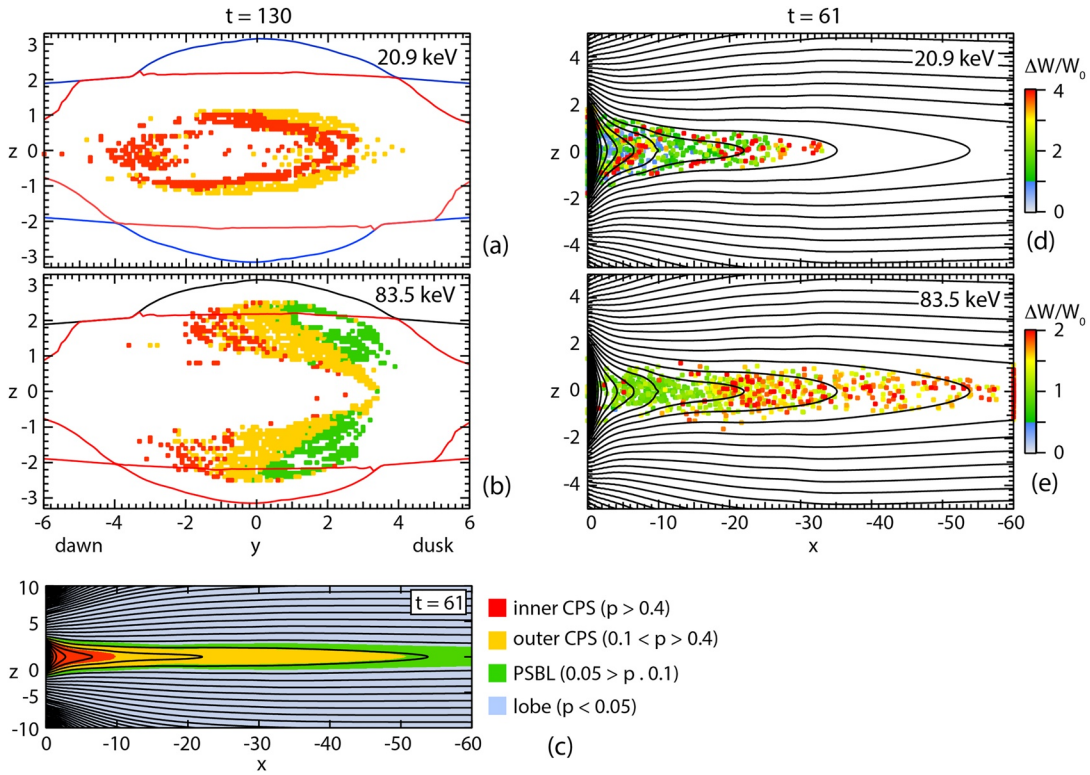

Figure 8. Origins of accelerated 20.9 and 83.5 keV protons contributing to enhanced fluxes in the $x = -30$ plane at $t = 130$. Panels a and b show top fluxes in the velocity distributions of Figures 7b and 7f, with color indicating the origin as defined by the initial pressure (panel c). Panels d and e show the source locations of the particles projected into the x, z plane with color now indicating the relative energy gain, together with the magnetic flux contours at $t = 61$. Black and red contours in panels a and b again indicate the topological boundaries with the red line showing the outer boundary of closed plasmoid field lines and the black line the inner lobe boundary.

includes a small net cross-tail magnetic field (guide field) of a few percent of the lobe field, which breaks the mirror symmetry but apparently has no significant influence on the dynamic evolution. The simulation does not include a distant reconnection site. Therefore the investigated properties are purely the consequences of near-Earth reconnection and tailward plasmoid ejection; they do not include fast impulsive or convective earthward flows in the mid tail, which in observations may constitute about one half of the fast flows at lunar distance (Kiehas et al., 2018).

Concerning the MHD simulation, we would like to point out a few results. First, although the maximum tailward speeds are comparable to the earthward speeds in the inner tail, the maximum integrated cross-tail electric fields in the departing plasmoid are smaller than in the dipolarizing flux bundle moving earthward, yielding cross-tail voltages of approximately 50–80 keV compared to ~200 keV on the earthward side for the chosen parameters (Section 2). Second, the simulation does not yield a unique plasmoid width. The helical field lines close to the core of the plasmoid tend to extend more widely in y, and are more tightly wound, than the field lines on the outside, even when both kinds are still connected to the Earth at both ends. The narrower width of the outer structure is related to the width of the fast tailward beam and the associated limited width of fast reconnection.

We have focused on two final energies, 20.9 and 83.5 keV, the latter being slightly above the maximum energy gain from a crossing of the dawn-dusk electric field region associated with the reconnection site and the departing plasmoid, which is about 50–80 keV, based on the chosen dimensional units. We note again, that our results can still be scaled to different cases by choosing different normalization parameters. For instance, increasing the magnetic field unit by, say, a factor of 2 and reducing the time unit by 1/2 leaves the dimensionless orbit results unchanged but would increase the two chosen particle energies to 83.5 and 334 keV, respectively, and the cross tail voltage to ~200–320 kV.

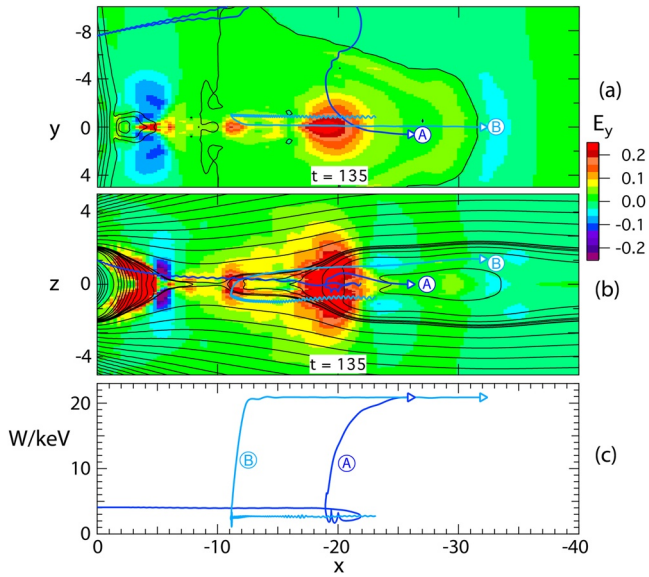

Figure 9. Typical orbits of accelerated protons (dark and light blue curves, labeled A and B) contributing to enhanced 20.9 keV fluxes at $t = 130$ in Figure 7b: (a) projection into the x, z plane, (b) projection into the x, y plane. The orbits are superposed on snapshots of the cross-tail electric field E_y at $t = 130$; the final locations are indicated by small triangles. Panel (c) shows the particle energies above the location in x.

The following are major conclusions:

1. The ion acceleration is primarily due to direct acceleration across the tail from the inductive electric field associated with the dynamic tail evolution, involving near-tail reconnection and plasmoid ejection. This electric field is dominated by the resistive term only in the immediate vicinity of the x-line but elsewhere given by the motional $-\mathbf{v} \times \mathbf{B}$ field. The maximum acceleration is thus limited by the maximum cross-tail voltage $\int E_y dy$. This is about 80 kV for the chosen parameters but might be higher in different scenarios when different parameters (larger B_n and/or larger L_n) were more appropriate. This is lower than what we found for the earthward side. The primary reason is that in our simulation, the B_z field associated with the plasmoid is smaller than the field in the earthward propagating dipolarization front. Our simulation does not exhibit the enhanced fields of anti-dipolarization fronts, which are occasionally observed on the tailward side (Li et al., 2014) and could possibly lead to larger cross-tail voltages.
2. The spatial distributions in the x, z plane show the boundary layers of tailward streaming energetic ions, as expected from ISEE-3 observations (Hones, Birn, et al. (1984); Richardson & Cowley, 1985; Scholer et al., 1983; Scholer, 1984).
3. The distributions in the x, y plane are more complicated, but preferentially duskward, as to be expected from the acceleration in that direction.
4. Acceleration of ions may occur anywhere across the tailward propagating electric field pulse associated with the plasmoid departure. Different branches of accelerated ions in the equatorial plane can be attributed to different acceleration locations in x. However, field-aligned beams near the plasma sheet boundary are primarily accelerated near the x-line in the near tail.
5. The accelerated particles originate mostly from the CPS; this is a main difference from the results of Scholer and Jamitzky (1989). It is probably related to the fact that the Scholer and Jamitzky (1989) simulation was two-dimensional without cross-tail variation, while ours is three-dimensional yielding a finite cross-tail extent of the reconnection site, the ejected plasmoid, and the associated electric fields. In this paper we did not

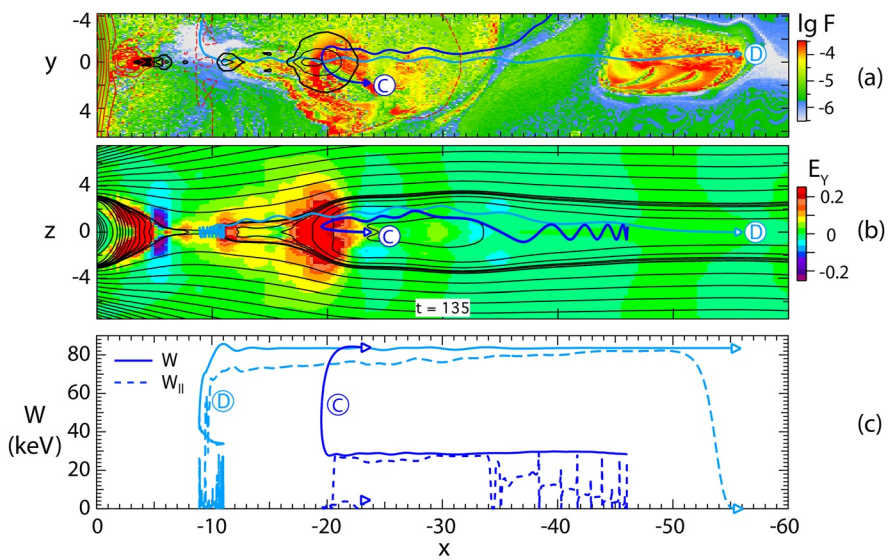

Figure 10. Same as Figure 9 but for protons contributing to enhanced fluxes at 83.5 keV. Panel a shows the color-coded particle fluxes in the x, y plane as in Figure 6d while panel b shows the electric field E_y. Panel c shows the particle energies as function of x as solid lines and the field-aligned contributions as dashed lines.

explore entry and acceleration mechanisms for different ion species. However, the two possible entry ways might explain the apparent mixing of ions of ionospheric and solar wind origin observed by Lui et al. (1998).

Data Availability Statement

Simulation results are available under doi:10.5281/zenodo.5206828.

Acknowledgments
The simulation work was performed at Los Alamos under the auspices of the US Department of Energy, supported by NASA grants 80NSSC18K0834, 80NSSC18K1452, and NSF Grant 1602655. IJC and DLT were supported by the Magnetospheric Multiscale (MMS) mission of NASA's Science Directorate Heliophysics Division via subcontract to the Southwest Research Institute (NNG04EB99C). AR was supported by NASA LWS Grant 80NSSC20K1788 and the HERMES DRIVE Science center (Grant 80NSSC20K0604). JAS was supported by NASA's MMS Guest Investigator Program Grant 80NSSC18K1363.

References

Angelopoulos, V. (2008). The THEMIS mission. *Space Science Reviews*, *141*, 5–34. https://doi.org/10.1007/s11214-008-9336-1
Angelopoulos, V. (2011). The ARTEMIS mission. *Space Science Reiews*, *165*, 3–25. https://doi.org/10.1007/s11214-010-9687-2
Angelopoulos, V., Mitchell, D. G., Williams, D. J., McEntire, R. W., Lui, A. T. Y., Decker, R. B., et al. (1995). Growth and evolution of a plasmoid associated with a small, isolated substorm: IMP 8 and GEOTAIL measurements in the magnetotail. *Geophysical Research Letters*, *22*(22), 3011–3014. https://doi.org/10.1029/95GL03133
Armstrong, T. P., & Krimigis, S. M. (1968). Observations of protons in the magnetosphere and magnetotail with Explorer 33. *Journal of Geophysical Research*, *73*(1), 143–152. https://doi.org/10.1029/JA073i001p00143
Atkinson, G. (1966). A theory of polar substorms. *Journal of Geophysical Research*, *71*, 5157–5164. https://doi.org/10.1029/jz071i021p05157
Atkinson, G. (1967). Polar magnetic substorms. *Journal of Geophysical Research*, *72*, 1491–1494. https://doi.org/10.1029/jz072i005p01491
Baker, D. N., Bame, S. J., Birn, J., Feldman, W. C., Gosling, J. T., Hones, E. W., Jr, et al. (1984). Direct observations of passages of the distant neutral line (80-140 R_E) following substorm onsets: ISEE-3. *Geophysical Research Letters*, *11*(10), 1042–1045. https://doi.org/10.1029/GL011i010p01042
Baker, D. N., Pulkkinen, T. I., Angelopoulos, V., Baumjohann, W., & McPherron, R. L. (1996). Neutral line model of substorms: Past results and present view. *Journal of Geophysical Research*, *101*, 12975–13010. https://doi.org/10.1029/95ja03753
Bame, S. J., Anderson, R. C., Asbridge, J. R., Baker, D. N., Feldman, W. C., Gosling, J. T., et al. (1983). Plasma regimes in the deep geomagnetic tail: ISEE 3. *Geophysical Research Letters*, *10*(9), 912–915. https://doi.org/10.1029/GL010i009p00912
Behannon, K. W. (1968). Mapping of the Earth's bow shock and magnetic tail by Explorer 33. *Journal of Geophysical Research*, *73*(3), 907–930. https://doi.org/10.1029/JA073i003p00907
Bhattacharjee, A., Huang, Y.-M., Yang, H., & Rogers, B. (2009). Fast reconnection in High-Lundquist-Number plasmas due to the plasmoid instability. *Physics of Plasmas*, *16*(11), 112102. https://doi.org/10.1063/1.326410310.1063/1.3264103
Birn, J., & Hesse, M. (1996). Details of current disruption and diversion in simulations of magnetotail dynamics. *Journal of Geophysical Research*, *101*(A7), 15345–15358. https://doi.org/10.1029/96ja00887
Birn, J., Nakamura, R., Panov, E., & Hesse, M. (2011). Bursty bulk flows and dipolarization in MHD simulations of magnetotail reconnection. *Journal of Geophysical Research*, *116*, A01210. https://doi.org/10.1029/2010JA016083
Birn, J., Thomsen, M. F., & Hesse, M. (2004). Acceleration of oxygen ions in the dynamic magnetotail. *Annales Geophysicae*, *22*(4), 1305–1315. https://doi.org/10.5194/angeo-22-1305-2004
Burch, J. L., Moore, T. E., Torbert, R. B., & Giles, B. L. (2016). Magnetospheric Multiscale: Overview and science objectives. *Space Science Reviews*, *199*, 5–21. https://doi.org/10.1007/s11214-015-0164-9
Chen, L.-J., Bhattacharjee, A., Puhl-Quinn, P. A., Yang, H., Bessho, N., Imada, S., et al. (2008). Observation of energetic electrons within magnetic islands. *Nature Physics*, *4*(1), 19–23. https://doi.org/10.1038/nphys777
Christon, S. P., Mitchell, D. G., Williams, D. J., Huang, C. Y., Frank, L. A., & Eastman, T. E. (1988). Energy spectra of plasma sheet ions and electrons from eV/e to ~1 MeV during plasma sheet temperature transitions. *Journal of Geophysical Research*, *93*, 2562–2572. https://doi.org/10.1029/ja093ia04p02562
Christon, S. P., Williams, D. J., Mitchell, D. G., Frank, L. A., & Huang, C. Y. (1989). Spectral characteristics of plasma sheet ion and electron populations during undisturbed geomagnetic conditions. *Journal of Geophysical Research*, *94*(A10), 13409–13424. https://doi.org/10.1029/ja094ia10p13409
Cowley, S. W. H., Hynds, R. J., Richardson, I. G., Daly, P. W., Sanderson, T. R., Wenzel, K.-P., et al. (1984). Energetic ion regimes in the deep geomagnetic tail: ISEE-3. *Geophysical Research Letters*, *11*(3), 275–278. https://doi.org/10.1029/GL011i003p00275
Curran, D. B., & Goertz, C. K. (1989). Particle distributions in a two-dimensional reconnection field geometry. *Journal of Geophysical Research*, *94*(A1), 272–286. https://doi.org/10.1029/ja094ia01p00272
Daly, P. W., Sanderson, T. R., & Wenzel, K.-P. (1984). Survey of energetic (E 35 keV) ion anisotropies in the deep geomagnetic tail. *Journal of Geophysical Research*, *89*(A12), 10733–10739. https://doi.org/10.1029/JA089iA12p10733
Daughton, W., Roytershteyn, V., Albright, B. J., Karimabadi, H., Yin, L., & Bowers, K. J. (2009). Transition from collisional to kinetic regimes in large-scale reconnection layers. *Physical Review Letters*, *103*, 1–4. https://doi.org/10.1103/physrevlett.103.065004
Drake, J. F., Swisdak, M., Che1, H., & Shay, M. A. (2006). Electron acceleration from contracting magnetic islands during reconnection. *Nature*, *443*, 553–556. https://doi.org/10.1038/nature05116
Eastwood, J. P., Phan, T.-D., Mozer, F. S., Shay, M. A., Fujimoto, M., Retinò, A., et al. (2007). Multi-point observations of the Hall electromagnetic field and secondary island formation during magnetic reconnection. *Journal of Geophysical Research*, *112*, A06235. https://doi.org/10.1029/2006JA012158
Escoubet, C. P., Fehringer, M., & Goldstein, M. L. (2001). The Cluster mission. *Annals of Geophysics*, *19*, 1197–1200. https://doi.org/10.5194/angeo-19-1197-2001
Fennell, J. F. (1970). Observations of proton bursts in the magnetotail with Explorer 35. *Journal of Geophysical Research*, *75*(34), 7048–7059. https://doi.org/10.1029/JA075i034p07048
Galeev, A. A. (1979). Reconnection in the magnetotail. *Space Science Reviews*, *23*, 411–425. https://doi.org/10.1007/bf00172248
Grigorenko, E. E., Runov, A., Angelopoulos, V., & Zelenyi, L. M. (2019). Particle beams in the vicinity of magnetic separatrix according to near-lunar ARTEMIS observations. *Journal of Geophysical Research: Space Physics*, *124*(3), 1883–1903. https://doi.org/10.1029/2018JA026160
Håland, S., Søraas, F., & Ullaland, S. (1999). Propagation velocities and dimensions of plasmoid structures in the near-earth magnetotail. *Geophysical Research Letters*, *26*(21), 3269–3272. https://doi.org/10.1029/1999GL003609

Hones, E. W., Jr. (1977). Substorm processes in the magnetotail: Comments on "On hot tenuous plasmas, fireballs, and boundary layers in the Earth's magnetotail" by frank et al. *Journal of Geophysical Research*, *82*, 5633–5640. https://doi.org/10.1029/ja082i035p05633

Hones, E. W., Jr, Baker, D. N., Bame, S. J., Feldman, W. C., Gosling, J. T., McComas, D. J., et al. (1984). Structure of the magnetotail at 220 R_E and its response to geomagnetic activity. *Geophysical Research Letters*, *11*(1), 5–7. https://doi.org/10.1029/GL011i001p00005

Hones, E. W., Jr, Birn, J., Baker, D. N., Bame, S. J., Feldman, W. C., McComas, D. J., et al. (1984). Detailed examination of a plasmoid in the distant magnetotail with isee 3. *Geophysical Research Letters*, *11*(10), 1046–1049. https://doi.org/10.1029/GL011i010p01046

Ieda, A., Machida, S., Mukai, T., Saito, Y., Yamamoto, T., Nishida, A., et al. (1998). Statistical analysis of the plasmoid evolution with Geotail observations. *Journal of Geophysical Research*, *103*(A3), 4453–4465. https://doi.org/10.1029/97JA03240

Kiehas, S. A., Runov, A., Angelopoulos, V., Hietala, H., & Korovinskiy, D. (2018). Magnetotail fast flow occurrence rate and dawn-dusk asymmetry at $x_{GSM} \sim -60\ R_E$. *Journal of Geophysical Research: Space Physics*, *123*, 1767–1778. https://doi.org/10.1002/2017JA024776

Kokubun, S., Yamamoto, T., Acuña, M. H., Hayashi, K., Shiokawa, K., & Kawano, H. (1994). The GEOTAIL magnetic field experiment. *Journal of Geomagnetism and Geoelectricity*, *46*(1), 7–21. https://doi.org/10.5636/jgg.46.7

Li, S.-S., Liu, J., Angelopoulos, V., Runov, A., Zhou, X.-Z., & Kiehas, S. A. (2014). Antidipolarization fronts observed by ARTEMIS. *Journal of Geophysical Research: Space Physics*, *119*, 7181–7198. https://doi.org/10.1002/2014JA020062

Lui, A. T. Y., Williams, D. J., McEntire, R. W., Christon, S. P., Eastman, T. E., Yamamoto, T., & Kokubun, S. (1998). Ion composition and charge state of energetic particles in flux ropes/plasmoids. *Journal of Geophysical Research*, *103*(A3), 4467–4475. https://doi.org/10.1029/97JA02256

Machida, S., Ieda, A., Mukai, T., Saito, Y., & Nishida, A. (2000). Statistical visualization of Earth's magnetotail during substorms by means of multidimensional superposed epoch analysis with geotail data. *Journal of Geophysical Research*, *105*(A11), 25291–25303. https://doi.org/10.1029/2000JA900064

Machida, S., Mukai, T., Saito, Y., Obara, T., Yamamoto, T., Nishida, A., et al. (1994). GEOTAIL low energy particle and magnetic field observations of a plasmoid at $x_{GSM} = -142R_E$. *Geophysical Research Letters*, *21*(25), 2995–2998. https://doi.org/10.1029/94GL02241

McPherron, R. L., Russell, C. T., & Aubry, M. A. (1973). Satellite studies of magnetospheric substorms on August 15, 1968, 9, Phenomenological model for substorms. *Journal of Geophysical Research*, *78*, 3131–3149. https://doi.org/10.1029/ja078i016p03131

Mihalov, J. D., Colburn, D. S., Currie, R. G., & Sonett, C. P. (1968). Configuration and reconnection of the geomagnetic tail. *Journal of Geophysical Research*, *73*(3), 943–959. https://doi.org/10.1029/JA073i003p00943

Mihalov, J. D., & Sonett, C. P. (1968). The cislunar geomagnetic tail gradient in 1967. *Journal of Geophysical Research*, *73*(21), 6837–6841. https://doi.org/10.1029/JA073i021p06837

Moldwin, M. B., & Hughes, W. J. (1992). On the formation and evolution of plasmoids: A survey of ISEE 3 geotail data. *Journal of Geophysical Research*, *97*(A12), 19259–19282. https://doi.org/10.1029/92JA01598

Mukai, T., Machida, S., Saito, Y., Hirahara, M., Terasawa, T., Kaya, N., & Nishida, A. (1994). The low-energy particle (LEP) experiment onboard the GEOTAIL satellite. *Journal of Geomagnetism and Geoelectricity*, *46*(10), 909. https://doi.org/10.5636/jgg.46.669

Nagai, T., Takahashi, K., Kawano, H., Yamamoto, T., Kokubun, S., & Nishida, A. (1994). Initial GEOTAIL survey of magnetic substorm signatures in the magnetotail. *Geophysical Research Letters*, *21*(25), 2991–2994. https://doi.org/10.1029/94GL01420

Ness, N. F., Behannon, K. W., Scearce, C. S., & Cantarano, S. C. (1967a). Early results from the magnetic field experiment on lunar explorer 35. *Journal of Geophysical Research*, *72*(23), 5769–5778. https://doi.org/10.1029/JZ072i023p05769

Ness, N. F., Behannon, K. W., Scearce, C. S., & Cantarano, S. C. (1967b). Eobservations of Earth's magnetic tail and neutral sheet at 510,000 kilometers by explorer 33. *Journal of Geophysical Research*, *72*, 927–933. https://doi.org/10.1029/JZ072i003p00927

Nishida, A. (1994). The Geotail mission. *Geophysical Research Letters*, *21*(25), 2871–2873. https://doi.org/10.1029/94GL01223

Richardson, I. G., & Cowley, S. W. H. (1985). Plasmoid-associated energetic ion bursts in the deep geomagnetic tail: Properties of the boundary layer. *Journal of Geophysical Research*, *90*(A12), 12133–12158. https://doi.org/10.1029/JA090iA12p12133

Richardson, I. G., Cowley, S. W. H., Hones, E. W., Jr, & Bame, S. J. (1987). Plasmoid-associated energetic ion bursts in the deep geomagnetic tail: Properties of plasmoids and the postplasmoid plasma sheet. *Journal of Geophysical Research*, *92*(A9), 9997–10013. https://doi.org/10.1029/JA092iA09p09997

Runov, A., Angelopoulos, V., Artemyev, A., Lu, S., & Zhou, X.-Z. (2018). Near-Earth reconnection ejecta at lunar distances. *Journal of Geophysical Research: Space Physics*, *123*(4), 2736–2744. https://doi.org/10.1002/2017JA025079

Sarris, E. T., Krimigis, S. M., & Armstrong, T. P. (1976). Observations of magnetospheric bursts of high-energy protons and electrons at ∼35 R_E with Imp 7. *Journal of Geophysical Research*, *81*(13), 2341–2355. https://doi.org/10.1029/JA081i013p02341

Sarris, E. T., Krimigis, S. M., Iijima, T., Bostrom, C. O., & Armstrong, T. P. (1976). Location of the source of magnetospheric energetic particle bursts by multispacecraft observations. *Geophysical Research Letters*, *3*(8), 437–440. https://doi.org/10.1029/GL003i008p00437

Schindler, K. (1974). A theory of the substorm mechanism. *Journal of Geophysical Research*, *79*, 2803–2810. https://doi.org/10.1029/ja079i019p02803

Scholer, M. (1984). Energetic ions and electrons and their acceleration processes in the magnetotail. In E. W. Hones, Jr. (Ed.), *Magnetic reconnection in space and laboratory plasmas* (pp. 216–227). American Geophysical Union. https://doi.org/10.1029/gm030p0216

Scholer, M., Gloeckler, G., Hovestadt, D., Ipavich, F. M., Klecker, B., & Fan, C. Y. (1983). Anisotropies and flows of suprathermal particles in the distant magnetotail: ISEE 3 observations. *Geophysical Research Letters*, *10*(12), 1203–1206. https://doi.org/10.1029/GL010i012p01203

Scholer, M., Gloeckler, G., Hovestadt, D., Klecker, B., & Ipavich, F. M. (1984). Characteristics of plasmoidlike structures in the distant magnetotail. *Journal of Geophysical Research*, *89*(A10), 8872–8876. https://doi.org/10.1029/JA089iA10p08872

Scholer, M., Gloeckler, G., Klecker, B., Ipavich, F. M., Hovestadt, D., & Smith, E. J. (1984). Fast moving plasma structures in the distant magnetotail. *Journal of Geophysical Research*, *89*(A8), 6717–6727. https://doi.org/10.1029/JA089iA08p06717

Scholer, M., & Jamitzky, F. (1987). Particle orbits during the development of plasmoids. *Journal of Geophysical Research*, *92*(12), 12,181–12,186. https://doi.org/10.1029/ja092ia11p12181

Scholer, M., & Jamitzky, F. (1989). Plasmoid-associated energetic ion bursts in the deep magnetotail: Numerical modeling of the boundary layer. *Journal of Geophysical Research*, *94*(A3), 2459. https://doi.org/10.1029/ja094ia03p02459

Sergeev, V. A., Pellinen, R. J., & Pulkkinen, T. I. (1996). Steady magnetospheric convection: A review of recent results. *Space Science Reviews*, *75*, 551–604. https://doi.org/10.1007/bf00833344

Slavin, J. A., Fairfield, D. H., Kuznetsova, M. M., Owen, C. J., Lepping, R. P., Taguchi, S., et al. (1998). ISTP observations of plasmoid ejection: IMP 8 and geotail. *Journal of Geophysical Research*, *103*(A1), 119–133. https://doi.org/10.1029/97JA02136

Slavin, J. A., Hesse, M., Owen, C. J., Taguchi, S., Fairfield, D. H., Lepping, R. P., et al. (1999). Dual spacecraft observations of lobe magnetic field perturbations before, during and after plasmoid release. *Geophysical Research Letters*, *26*(19), 2897–2900. https://doi.org/10.1029/1999GL003606

Slavin, J. A., Lepping, R. P., Gjerloev, J., Fairfield, D. H., Hesse, M., Owen, C. J., & Mukai, T. (2003). Geotail observations of magnetic flux ropes in the plasma sheet. *Journal of Geophysical Research*, *108*(A1), 1015. https://doi.org/10.1029/2002JA009557

Slavin, J. A., Tsurutani, B. T., Smith, E. J., Jones, D. E., & Sibeck, D. G. (1983). Average configuration of the distant (220 R_E) magnetotail: Initial ISEE-3 magnetic field results. *Geophysical Research Letters*, *10*(10), 973–976. https://doi.org/10.1029/GL010i010p00973

Sun, W. J., Slavin, J. A., Tian, A. M., Bai, S. C., Poh, G. K., Akhavan-Tafti, M., et al. (2019). MMS study of the structure of ion-scale flux ropes in the Earth's cross-tail current sheet. *Geophysical Research Letters*, *46*(12), 6168–6177. https://doi.org/10.1029/2019GL083301

Tsurutani, B. T., Slavin, J. A., Smith, E. J., Okida, R., & Jones, D. E. (1984). Magnetic structure of the distant geotail from -60 to -220 R_e: ISEE-3. *Geophysical Research Letters*, *11*(1), 1–4. https://doi.org/10.1029/GL011i001p00001

Tsurutani, B. T., & von Rosenvinge, T. T. (1984). ISEE-3 distant geotail results. *Geophysical Research Letters*, *11*(10), 1027–1029. https://doi.org/10.1029/GL011i010p01027

Tsyganenko, N. (1987). Global quantitative models of the geomagnetic field in the cislunar magnetosphere for different disturbance levels. *Planetary and Space Science*, *35*, 1347–1358. https://doi.org/10.1016/0032-0633(87)90046-8

Vasyliunas, V. (1968). Observations of low-energy electrons in the evening sector of the magnetosphere with OGO-1 and OGO-3. *Journal of Geophysical Research*, *73*, 2839–2884. https://doi.org/10.1029/ja073i009p02839

Zeleny, L., Lipatov, A., Lominadze, D., & Taktakishvili, A. (1984). The dynamics of the energetic proton bursts in the course of the magnetic field topology reconstruction in the earth's magnetotail. *Planetary and Space Science*, *32*(3), 313–324. https://doi.org/10.1016/0032-0633(84)90167-3

Zelenyi, L. M., Lominadze, J. G., & Taktakishvili, A. L. (1990). Generation of the energetic proton and electron bursts in planetary magnetotails. *Journal of Geophysical Research*, *95*(A4), 3883–3891. https://doi.org/10.1029/JA095iA04p03883

Zhong, Z., Zhou, M., Burch, J., Tang, R., Deng, X., Turner, D., & Khotyaintsev, Y. (2020). Direct evidence for electron acceleration within ion-scale flux rope. *Geophysical Research Letters*, *47*(1), e2019GL085141. https://doi.org/10.1029/2019gl085141

Zwickl, R. D., Baker, D. N., Bame, S. J., Feldman, W. C., Gosling, J. T., Hones, E. W., Jr, et al. (1984). Evolution of the earth's distant magnetotail: ISEE 3 electron plasma results. *Journal of Geophysical Research*, *89*(A12), 11007–11012. https://doi.org/10.1029/JA089iA12p11007